Synthesis, Spectroscopic Characterization and Applications of Tin Dioxide



Hawazin Alghamdi, Benjamin Concepcion, Shankar Baliga, and Prabhakar Misra

Abstract Metal oxides are useful for the detection and sensing of combustible and toxic gases, and for use in lithium batteries and solar cells. The present study focuses on the spectroscopic investigation of commercial and in-house laboratory synthesized tetragonal tin dioxide (SnO₂), aimed at studying its physical and chemical properties at nanoscale levels and in bulk. We have investigated the pure powder form and thin films prepared on two different types of substrate, silicon and UV-Quartz, each with five different thicknesses (i.e. 41, 78, 96.5, 373, and 908 nm). Raman spectroscopy with two different laser excitation wavelengths, namely 780 and 532 nm, has been used to investigate the various SnO₂ vibrational modes. Thermal effects on the primary vibrational features in the Raman spectra have been studied in the range 30–170 °C. X-ray diffraction (XRD) spectra have been recorded to confirm the rutile structure of tin dioxide and to obtain information on the spherical grain particle size of SnO₂ with EDS analysis for the thin film samples. Scanning Electron Microscope (SEM) images have been recorded in order to understand the morphology of the particles of SnO₂ at the nanoscale level. In addition, FT-IR spectra have been obtained to study the IR-active vibrational modes for the bulk and thin film samples on the two substrates. Moreover, UV-VIS spectra have been employed to determine the energy band gap for the SnO₂ film samples by an efficient process facilitated by a Tauc plot technique utilizing an in-house developed python script.

Keywords Tin dioxide · Raman scattering · FT-IR spectroscopy · X-ray diffraction · Scanning Electron Microscopy (SEM) · UV-VIS spectroscopy · Gas sensor · Solar cells · Li-ion batteries · Molecular Dynamics (MD) simulation · Tauc plot

H. Alghamdi · P. Misra (⊠)

Laser Spectroscopy Laboratory, Department of Physics & Astronomy, Howard University, Washington, DC 20059, USA

e-mail: pmisra@howard.edu

B. Concepcion

Department of Physics, University of California, Berkeley, CA 94720, USA

S. Baliga

General Monitors, Lake Forest, CA 92630, USA

© Springer Nature Switzerland AG 2021 N. M. Mubarak et al. (eds.), *Contemporary Nanomaterials in Material Engineering Applications*, Engineering Materials, https://doi.org/10.1007/978-3-030-62761-4_11

1 Introduction

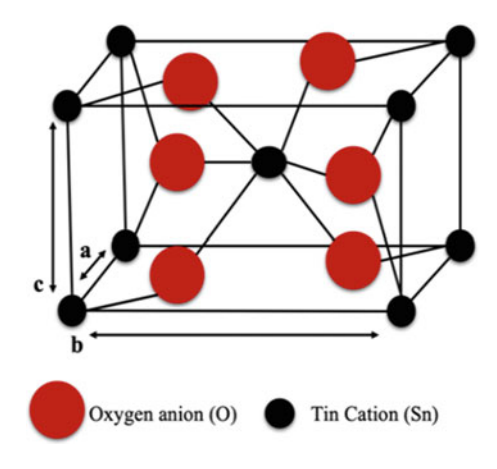
1.1 Metal Oxides

Metal oxides play a crucial role in applications in a variety of diverse fields, such as material science, inorganic chemistry, condensed matter physics, geology, electrical engineering and mechanical engineering [19]. They also have exceptional potential as base materials in developing leading-edge technologies. In recent years, extensive research effort has been directed towards metal oxides covering a range of applications in frontier areas in optoelectronics and device engineering. Depending on the nature of the surface, size and shape of the active metal oxide material(s), the response characteristics may differ. For example, the optical and electronic properties of such materials rely on the structure and spatial dimensions involved, whereas the physical and chemical properties of low-dimensional oxide materials can be remarkably altered by the Coulombic, Van der Waals, and interatomic coupling, due to the large number of atoms present on the surface in comparison to its bulk form. Therefore, significant interest exists in gaining a better understanding of a variety of low-dimensional materials in different forms, such as nanoparticles, nanowires, nanotubes, nanospheres, nanorods, nanoribbons, nanodisks and nanosheets. Enhanced insight into the thermal, electrical, and optical properties of such nanomaterials significantly contributes to improved fabrication of these materials with enhanced magnetic, electronic, and optoelectronic properties for a wide range of device applications [12]. Metal oxides are considered flexible and have been found useful for a host of applications relating to medical technology, water treatment, air pollutant reduction, purification of industrial and military polluted soils, and in personal care products [9].

1.2 Tin Dioxide

Mineral tin dioxide, often called stannic oxide or cassiterite (SnO_2) has the tetragonal crystalline structure, as do many other metal oxides. The rutile structure of SnO_2 has a tetragonal unit cell with P4₂/mnm space-group symmetry and lattice constants a=b=4.7374 Å and c=3.1864 Å [13]. This structure is the essential form among all other phases that can [14] be produced under high mechanical pressure from the commonly stable and available rutile phase. SnO_2 can have different phases of polymorphs, such as $CaCl_2$ -type (Pnnm), α -PbO₂-type (Pbcn), ZrO_2 -type orthorhombic phase I (Pbca), fluorite-type (Fm $\bar{3}$ m), pyrite-type (Pa $\bar{3}$), and a nine-fold coordination cotunnite-type orthorhombic phase II (Pnam) [12]. The unit cell of rutile-type SnO_2 contains six atoms; two of which are six-fold coordinated Sn and four are three-fold coordinated Sn in the chemical structure

Fig. 1 Unit cell rutile crystalline structure of SnO₂ [4]



O=Sn=O. Figure 1 shows the rutile tetragonal structure of tin dioxide, with six-anion oxygen surrounding a tin cation in the middle to form an imperfect octahedron of rutile structured tin atoms. The ionic radius of O^{2-} is 1.40 Å, while that for Sn^{4+} is 0.71 Å [14]. Each of the Sn atoms is located at the lattice vertices corresponding to the neighboring six O's of the distorted octahedral. The Sn atoms are located at (0,0,0) and $(\frac{1}{2} a,\frac{1}{2} c)$, while O atoms are located at \pm (ua,-ua,0) and $(\frac{1}{2} a,\frac{1}{2} a,\frac{1}{2} c)$ \pm (ua,ua,0), where u = 0.307 [3, 39]. SnO₂ is known for its unique properties, such as chemical and electrochemical stability, high optical transparency, nontoxicity, and efficient electron communication when doped [1]. It is a semiconductor with a wide direct band gap between the conduction and valence bands of approximately 3.6 eV [4]. It can be used effectively as a transparent conducting oxide gas sensor, a transparent electrode for lithium ion batteries, in solar cells, and finds potential applications in electrochromic devices [11, 58].

1.3 Methodology (Raman, FT-IR, XRD, SEM)

Raman Spectroscopy

The principle of Raman spectroscopy is based upon inelastic scattering of light incident on a sample. When a photon of frequency v_0 and energy hv_0 impinges on molecules of a sample, the molecules are transported to a *virtual energy state* for a short time interval, followed by the emission of a photon of frequency v_1 of energy hv_1 . The electron cloud of the sample interacts with the electric field of the monochromatic light and as a result the molecules get excited to a new rovibronic state and undergo a variation in their electric dipole-electric dipole *polarizability* that results in the Raman scattering effect. The intensities of the Raman lines are proportional to the change in the polarizability that the sample molecules experience, whereby the Raman spectrum (a plot of the scattering intensity versus frequency

shift) is a function of the rovibronic states of the molecules. The Raman shift $\Delta \nu$ in wavenumber units (cm⁻¹) is governed by the following equation:

$$\Delta v = [(1/\lambda_0) - (1/\lambda_1)] \tag{1}$$

where λ_0 is the wavelength of the excitation laser and λ_1 is the wavelength of the Raman spectral line. If the laser excitation wavelength (λ_0) and the Raman scattered wavelength (λ_1) are in nm, the Raman frequency shift (in cm⁻¹) is given by the equation:

$$\Delta \nu = \left[\left\{ 1/\lambda_0(\text{nm}) \right\} - \left\{ 1/\lambda_1(\text{nm}) \right\} \right] \times \left(10^7 \text{ nm} \right) / (\text{cm})$$
 (2)

The magnitudes of the Raman shifts are dictated by the polarizability of the electrons in the molecules.

Most of the excited molecules in the sample emit scattered radiation with a frequency that is equal to the incident radiation frequency and experience Rayleigh scattering (i.e. elastic scattering). However, a small portion of the scattered light also has a frequency different from the incident frequency and undergoes Raman scattering (i.e. inelastic scattering). If the final state of the molecule is higher than the initial energy state, the scattered photon will be shifted to a lower energy (lower wavenumber); this *downshift* defines the Stokes-shift. Conversely, when the final molecular state is lower in energy as compared to the initial state, the Raman scattered photon is shifted to a higher energy (higher wavenumber); the corresponding *upshift* is referred to as the anti-Stokes shift. The Raman spectra are therefore composed of both Stokes lines and anti-Stokes lines [7, 13, 38].

To characterize our tin dioxide samples, we used a DXRTM SmartRaman spectrometer with an excitation wavelength of 780 nm and $M^2 \le 1.5$ beam quality. We used the 780 nm excitation to measure the Stokes Raman spectra of the SnO₂ in bulk form at different temperatures with a high brightness single-mode diode laser. Figure 2 shows the instrument's internal optical layout with 780 nm excitation, where the laser is focused on the sample by an objective lens resulting in scattered light that is filtered (to remove the Rayleigh component) and subsequently imaged on to the CCD detector, yielding the Raman spectrum of our sample [8].

A heated cell is accommodated within the Raman SmartDXR[™] spectrometer sample compartment, in order to study the thermal effects on the recorded Raman spectra of the samples. We also used a Renishaw inVia Raman microscope with a laser wavelength of 532 nm to record the spectra of the tin dioxide samples. The powdered sample of SnO₂ (bulk) was compressed and transferred to the Ventacon[™] model H4-200 cell (shown in Fig. 3) that can be heated up to 200 °C. We utilized the heated cell to control the environment, while recording the Raman spectra of the samples simultaneously. The H4 cell system comprises of an oven fitted with a window at the front and a sealing system at the back. The sample is gently pressed to the rear face of the window with a stainless-steel rod.

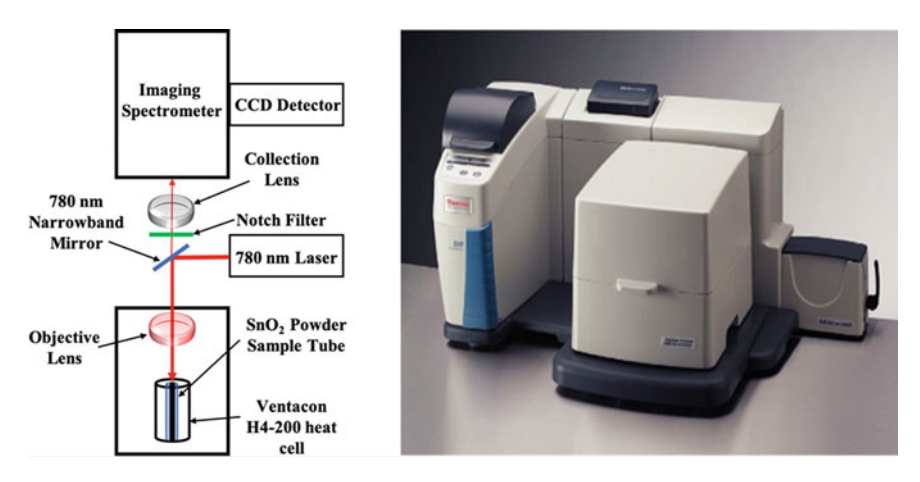


Fig. 2 Schematic of the Raman SmartDXRTM Spectrometer (left) and the Raman SmartDXRTM instrument (right). (Adapted from Casimir et al. [8])

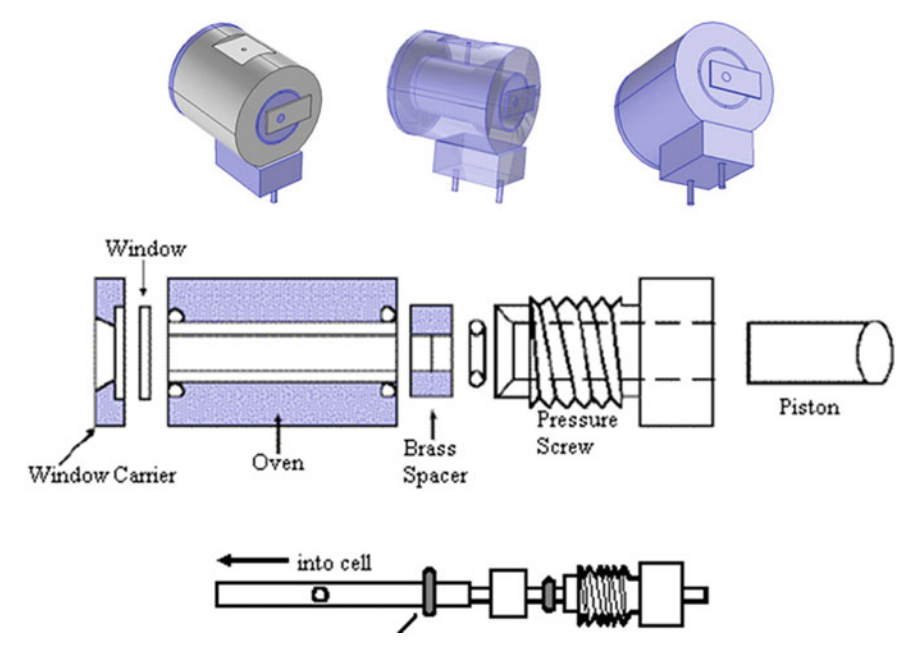


Fig. 3 (Top) An overview of the Ventacon[™] H4-200 heated cell; (middle) schematic cross-section of the heating cell; and (bottom) schematic cross-section of the cylindrical container of powdered samples. (Adapted from Casimir et al. [8])

Fourier Transform-Infrared Spectroscopy

When infrared radiation interacts with a molecule, some of the light gets absorbed. The molecule then vibrates and gets excited to a higher energy level. When the photon energy between the two permitted energy levels is coincident with the energy difference between the pair of levels, an absorption spectrum is recorded [38]. As a result, the resultant modes of vibration are infrared vibrations due to a change in the dipole moment [5].

In the Fourier Transform (IR) technique, a broadband light source shines into a Michelson interferometer. Different wavelengths are modulated at different rates and the beam exiting the spectrometer is a snapshot in time called an interferogram. Fourier transformation is used to convert the interferogram into an absorption spectrum of the signal at a series of discrete wavelengths.

We have collected FT-IR spectra of the samples using a Thermo Scientific[™] Nicolet[™] iS50 FT-IR Spectrometer. The iS50 FT-IR has a tungsten-halogen white light source with a Polaris[™] long-life IR source. The Attenuated Total Reflection (ATR) technique, which requires minimal sample preparation is used with a diamond crystal as shown in Fig. 4a–c. As shown in Fig. 4c, the ATR accessory operates by collecting the internally reflected infrared beam from an optically dense crystal (diamond). When the crystal comes into contact with the sample, the sample absorbs the light energy, and the evanescent wave is attenuated. Subsequently, the reflected

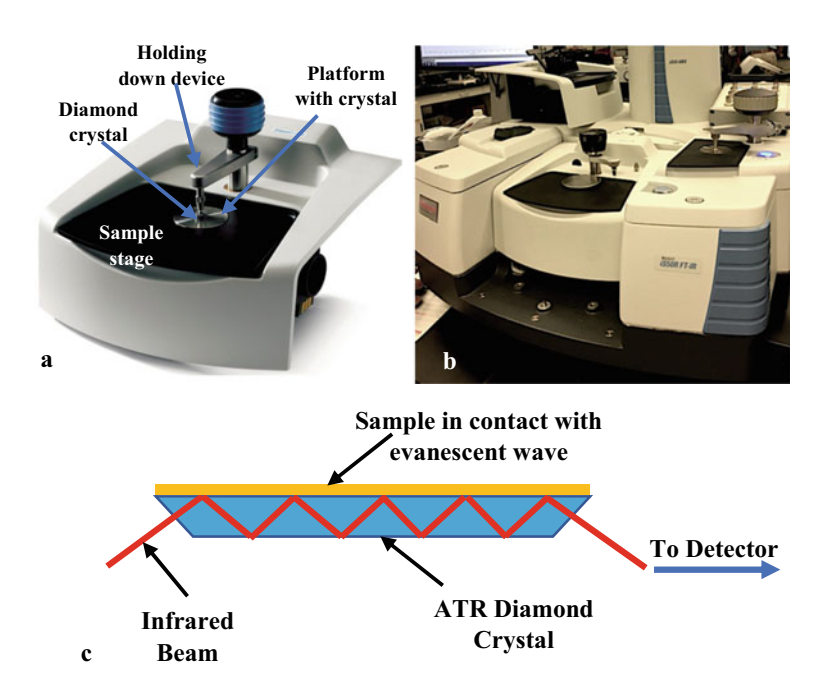


Fig. 4 a ATR sample stage; **b** ScientificTM NicoletTM iS50 FT-IR Spectrometer; **c** Schematic of ATR top plate. Thermo Fisher ScientificTM

energy goes to the IR spectrometer detector, which records the attenuated IR beam and generates the FT-IR spectra.

X-ray Diffraction

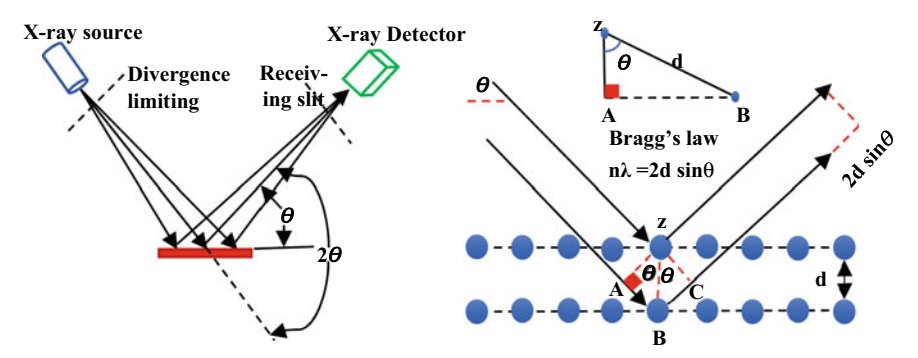
X-rays incident on a sample interact with the electrons of the array of atoms making up the material and experience *elastic scattering*. The resulting spherical waves undergo constructive interference to produce a diffraction pattern governed by Bragg's law:

$$2d \sin \theta = n \lambda \tag{3}$$

where d is the interplanar spacing in the nanomaterial sample, θ is the incident angle (as shown in Fig. 5) and λ is the wavelength of the incident X-ray radiation.

The X-Ray diffraction spectra of the SnO_2 samples were collected using a Thermo Scientific TM ARL TM EQUINOX 100 X-Ray diffractometer (XRD) (shown in Fig. 5). The size of the beam is approximately 5 mm \times 300 μ m, and a spinning stage for powder samples is used as illustrated in Fig. 5 (top). The EQUINOX curved detector can measure all diffraction peaks simultaneously across a wide angular range, which means it measures the whole 2θ range simultaneously and in real-time; no scanning is required. A regular X-ray diffraction instrument includes the X-ray source or tube,





 $\label{eq:Fig.5} \textbf{Fig. 5} \quad \text{(Top) Thermo Fisher Scientific} \\ \text{TM ARL} \\ \text{TM EQUINOX 100 X-Ray diffractometer; (bottom)} \\ \text{Schematic of X-ray diffraction}$

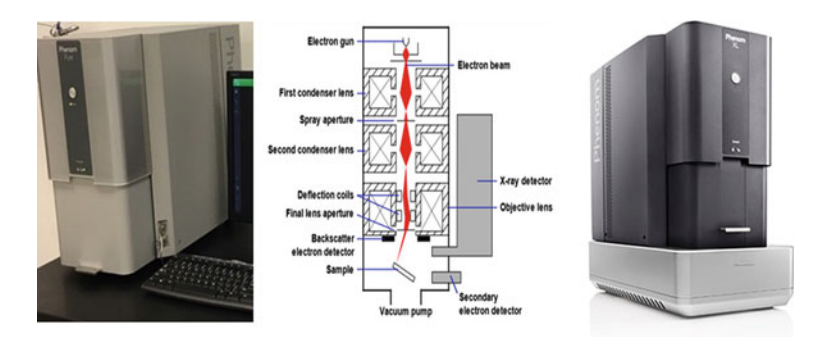


Fig. 6 (Left) Phenom Pure Scanning Electron Microscope (left); (Middle) Schematic of SEM adapted from Nanoscience Instruments, Inc. TM; (Right) Phenom XL Desktop Scanning Electron Microscope, Thermo Fisher Scientific TM

a sample stage, an optics receiver, and an X-ray detector. The ARLTM EQUINOX has the X-ray tube, and the X-ray detector is stationary. The only moving part in the XRD is the sample stage. The foundational principle behind XRD analysis is Bragg's law, which relates X-ray diffraction to the crystalline structure, allowing it to be determined experimentally. X-ray diffraction is a powerful technique used to study solid matter materials. Solid materials can either be crystallized, with the atoms organized in a regular or ordered manner, or amorphous, where the atoms are organized randomly. As shown in the schematic diagram, the angle between the X-ray source and the sample is θ , and the angle between the X-ray projection and the detector is 2θ [49].

Scanning Electron Microscope

A Scanning Electron Microscope (SEM) was utilized in order to investigate the surface morphology and topography of the bulk and film samples. Both Phenom Pure and Phenom XL desktop instruments have been utilized to study the samples. Both SEMs are shown in Fig. 6.

An electron gun emits electrons from a cathode, with variation in electron energy between hundreds of eV and few tens of keV. The electrons are subsequently accelerated by the gradient of an electric field and the beam passes through two condenser lenses and through an electromagnetic scanning coil to be focused on the sample that is placed in a vacuum chamber. The scanning coil directs the electron beam into the plane of the sample (i.e., x and y directions). The accelerated electrons with high energy create different types of emitted and scattered electrons from inelastic and elastic collisions occurring near the surface of the sample. The inelastic scattering of incident electrons produces secondary electrons that are detected by an electron detector [36].

2 Synthesis Methods and Characterization of SnO₂ Films

2.1 SnO₂ Powder and Thin Films on Si and UV-Quartz

Commercially purchased SnO₂ powder from SIGMA-ALDRICH with 325 mesh and 99.9% purity was used as a standard and for spectroscopic characterization. The powder sample was annealed at 1000 °C for 1 h. Thin films of SnO₂ on UV quartz and silicon wafers were created by radio frequency (RF) sputter deposition in an oxygen/argon mixed atmosphere. The sputtering target was a 6-inch diameter, ¹/₄ inch thick, ceramic target made from high purity tin dioxide. The deposited tin dioxide film thickness was monitored by sputter deposition onto a polished silicon substrate. A Filmetrics F20 instrument was used for curve fitting to calculate film thickness. Film thickness was varied by changing the sputter deposition time. UV-Quartz substrates were placed in the sputtering machine alongside the polished silicon thickness monitor substrate. UV-Quartz was chosen because it permitted transmission measurements in the UV at wavelengths as low as 190 nm with a UV spectrophotometer. The measurement of the SnO₂ band gap via UV transmission is described in Sect. 3.5.

3 Properties of SnO₂ via Spectroscopic Characterization

3.1 Temperature-Dependent Raman Spectroscopy of SnO₂

Raman spectroscopy is considered a versatile and sensitive technique to examine modifications in vibrational phonon modes crystallinity, surface and bulk atoms, disorder, and size effects in nanometric crystallites. The present research focuses on the vibrational modes of the rutile-structure of SnO_2 , where the normal modes with space-group symmetry of $P4_2/mnm$ (point group symmetry D_{4h}^{14}) at the Brillouin zone are given by Eq. (4) [35]:

$$\Gamma = 1A_{1g} + 1A_{2g} + 1B_{1g} + 1B_{2g} + 1E_g + 1A_{2u}$$

$$+ 2B_{1u} + 3E_u$$
(4)

where A_{1g} , B_{1g} , B_{2g} , and doubly degenerate E_g vibrational modes are Raman active, with the feature that the tin atoms remain at rest. A_{2u} and the triply degenerate E_u modes are active in IR (i.e. InfraRed light). The A_{2g} and the B_{1u} modes are considered silent (i.e., inactive optically) [13]. The vibrational modes are illustrated in Fig. 7 [4].

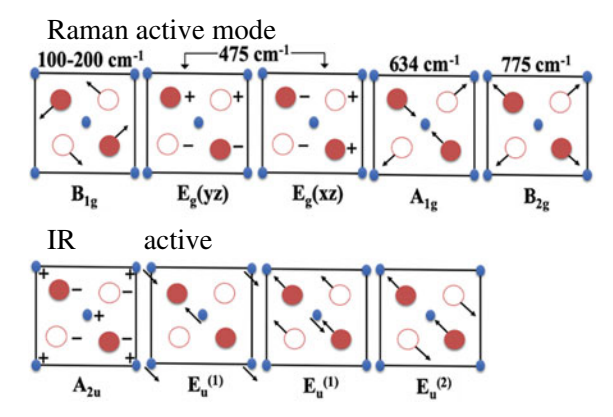


Fig. 7 Top view along the z-axis of rutile-structured SnO_2 optically active vibrational modes. The Sn atoms are indicated by (blue) dots, and O atoms are indicated by (red) dots: Raman active modes are shown with approximate wavenumber positions (top) and IR active modes (bottom), where the arrows represent the direction of movement in plane and (+ or -) represents the movement along the z-axis [13]

The B_{1g} Raman active mode, around 123 cm⁻¹, is not visible in many Raman spectrometers because its intensity is about three orders of magnitude less than that of the A_{2g} peak [31, 30]. The Raman spectra were collected by choosing a laser power of 10 mW and 25 μ m aperture slit at different increasing temperatures from 30 to 170 °C, in steps of 20 °C (as illustrated in Fig. 8). Temperature variations were accomplished by use of the Ventacon H4-200 heated cell (shown in Fig. 3).

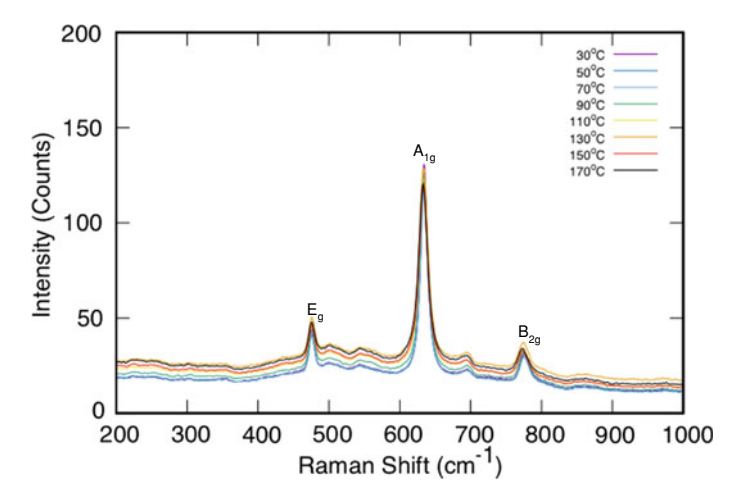


Fig. 8 Raman spectra of SnO_2 powder with 780 nm wavelength excitation as temperature varied between 30 and 170 °C

We have observed three of the four Raman active modes $(E_g, A_{1g} \text{ and } B_{2g})$ in the SnO₂ powder sample, where $A_{1g} = 634 \text{ cm}^{-1}$ is the most intense peak and represents the symmetric O–Sn–O stretching, $B_{2g} = 775 \text{ cm}^{-1}$ represents the antisymmetric O–Sn–O stretching, and $E_g = 475 \text{ cm}^{-1}$, which is doubly degenerate, represents the translational mode of SnO₂ [18, 47]. The B_{1g} mode cannot be observed with the rest of the Raman active phonons. In contrast to the other Raman active modes, the B_{1g} band dramatically increases in wavenumber with increasing temperature [45]. Other weak abnormal Raman modes are noticed at approximately 501.7, 544.0, and 695.3 cm⁻¹, which are similar to the reported bands of SnO₂ nanoribbons [53].

A comparison is done below for the two Raman active bands A_{1g} and B_{2g} with temperature variation in the range 30–170 °C, as shown in Fig. 9. The A_{1g} and B_{2g} bands decrease in wavenumber with increasing temperature, while the E_g mode appears to have almost no change as the temperature increases from 30 to 170 °C, as demonstrated in Fig. 10. Raman spectra of SnO_2 are modified based on the size, shape, and temperature of the crystal.

Increasing crystal size leads to a dramatically decreased wave number for the A_{1g} and B_{2g} bands, while the E_g band slightly decreases [31, 30]. At smaller crystal sizes, three bands are noticeable in the spectrum of SnO_2 powder, denoted as S_1 , S_2 , and S_3 as shown in Fig. 11. S_1 and S_2 slightly decrease in peak wave number with increasing crystal size, while S_3 has no reported shift. The amplitudes of these bands decrease as particle size increases. Some values for these peaks, when examined using a 488 nm Raman spectrometer, are shown in Table 1. Average crystal sizes are denoted by L and were determined through TEM measurements [14].

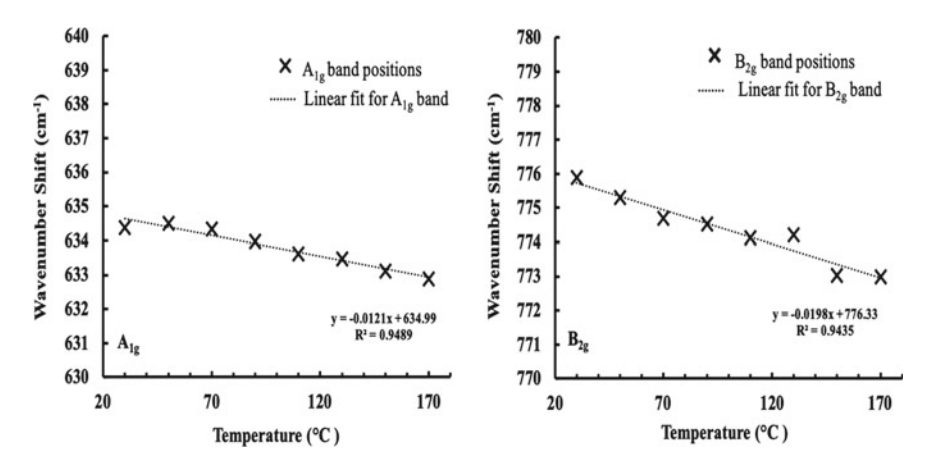


Fig. 9 Wavenumber shifts for the A_{1g} and B_{2g} vibration bands versus temperature in the range 30–170 °C

Fig. 10 Wavenumber variation for E_g vibration band versus temperature in the interval 30–170 °C

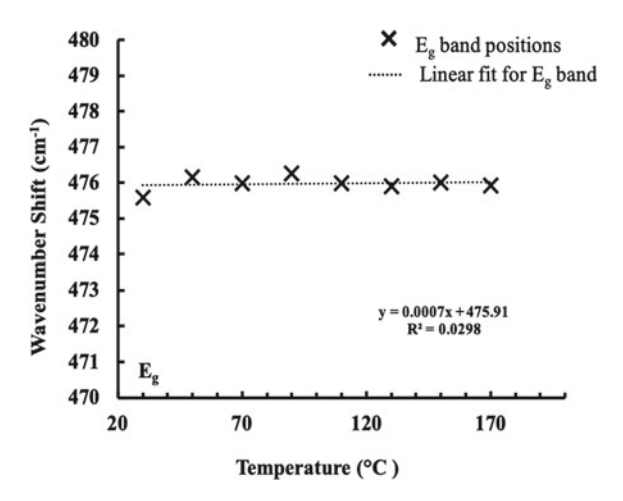


Fig. 11 Raman spectra of SnO_2 powder comprised of A_{1g} , B_{2g} , and E_g bands, along with S_1 , S_2 , and S_3 bands. Reproduced from Dieguez et al. [14], with permission of AIP Publishing

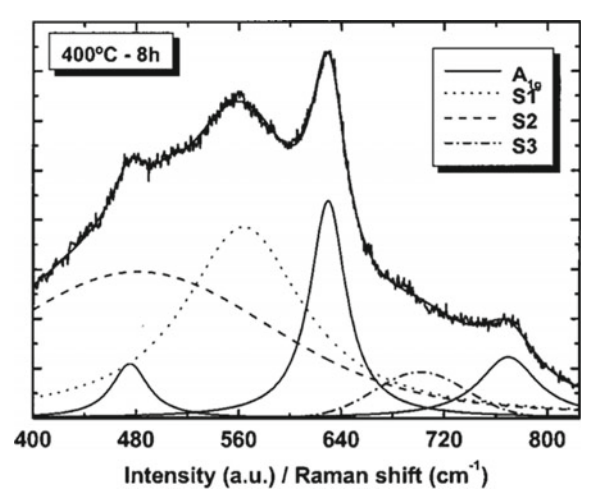


Table 1 Shifts in band wavenumber for SnO₂ powder based on changing particle size. Reproduced from Dieguez et al. [14], with permission of AIP Publishing

L (nm)	A _{1g}	B_{2g}	Eg	S1	S2	S3(A _{2u})
109.8	637.9	779.2	479.2			
56.6	637.9	778.9	479.5			
15.8	635.2	774.2	479.7	568.9	493.2	696.3
9.6	634.3	774.1	479.6	568.0	501.2	706.9
6.7	633.9	776.2	479.6	568.1	485.9	705.8
5.0	633.1	772.9		572.0	503.7	691.7
4.5	631.6	767.7		573.3	518.0	
3.5	631.5			575.8	541.7	

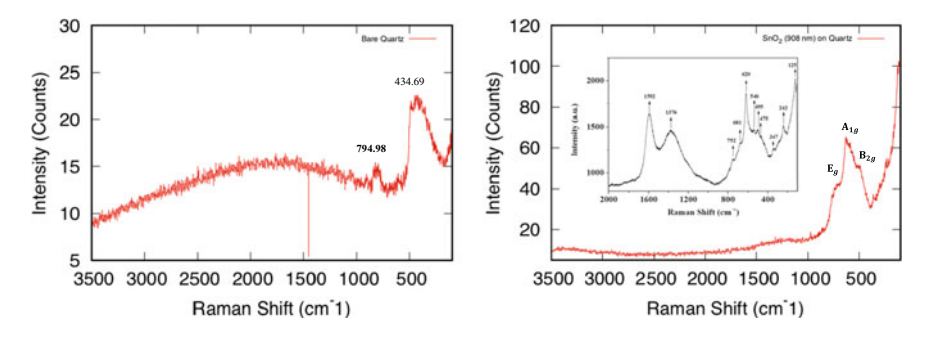


Fig. 12 DXR Raman spectra with 532 nm wavelength: Raman data of bare Quartz (left). Raman data of SnO₂ (908 nm) film thickness on Quartz compared with SnO₂/SiO₂ (right). The compared figure is retrieved from Ferreira et al. [18] with open access provided by SciELO Publishing

Thin films of SnO_2 will necessarily pick up spectroscopic characteristics from the media they are deposited on. Examples of such media are silicon and UV-Quartz; their pristine Raman spectra, along with their spectra with a 908 nm thick SnO_2 film, are shown in Fig. 12. A different wavelength of 532 nm was used because the 780 nm and the 514 nm wavelengths did not show any signs of the tin dioxide Raman bands.

The spectrum of the bare UV-Quartz has been collected with two pronounced features of quartz at (434.69 cm $^{-1}$) and in the interval (794.98–823.15 cm $^{-1}$), which approximately match the Raman peaks of borosilicate glass around (450–480 cm $^{-1}$) and (800 cm $^{-1}$), respectively [28]. The SnO $_2$ /Quartz (908 nm) film exhibited evidence of the Raman active modes around (627.07, 490.19, and 745.42 cm $^{-1}$), which resemble $A_{1g},\,E_g,\,$ and B_{2g} features, but are at somewhat different wavenenumbers, possibly due to the presence of the quartz substrate, a similar effect to what has been observed previously [18].

3.2 XRD Spectroscopy of SnO₂

X-ray diffraction (XRD) spectra were measured by utilizing the Thermo Fisher Scientific ARLTM EQUINOX 100 X-Ray diffractometer with a Cu–K α monochromatic radiation source with wavelength $\lambda=1.5406$ Å. The size of the beam is roughly 5 mm \times 300 μ m, with a spinning stage for powder sample loading. The spectra were collected in the range of $2\theta=20-80^\circ$. The XRD patterns for tin dioxide in powder form with 325 mesh, 99.9% trace metals, were recorded with 2 peak values and the associated numbers of Miller Indices (*hkl*) as 26.78° (110), 34.04° (101), 38.25° (200), 51.98° (211), 55.01° (220), 62.13° (310), 64.97° (112), and 66.15° (301), respectively, as shown in Fig. 13, which agree with Patil et al. [43] and Ferreira et al. [18].

The XRD spectra confirm the rutile tetragonal structure of SnO₂. XRD patterns for SnO₂ thin films were collected with thickness values of 41, 78, 96.5, 373, and

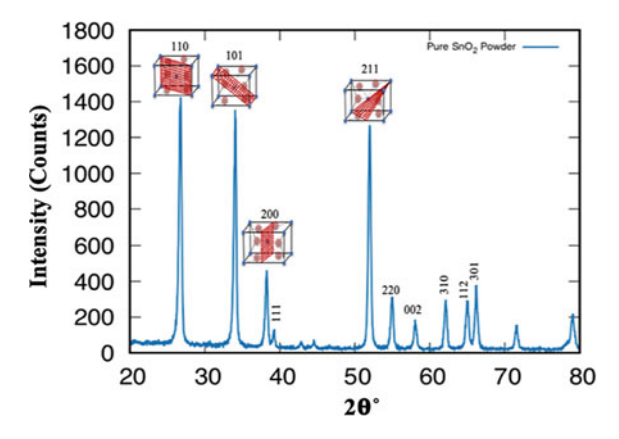


Fig. 13 XRD pattern of SnO₂ powder

908 nm, along with a bare double polished silicon wafer to act as a control. Figure 14 shows the XRD spectra of tin dioxide thin films over the range of $2\theta=0$ –80°. For the bare silicon wafer substrate, we can see the broad peak in the range $2\theta=5$ –20° approximately. The peak looks shifted in comparison to Su et al. [51] where they have the range to be $2\theta=10$ –20°.

For the lowest ratio thickness of the film (i.e., 41 nm), we can observe properties similar to the silicon substrate, except for a small hump around 26.2° that matches

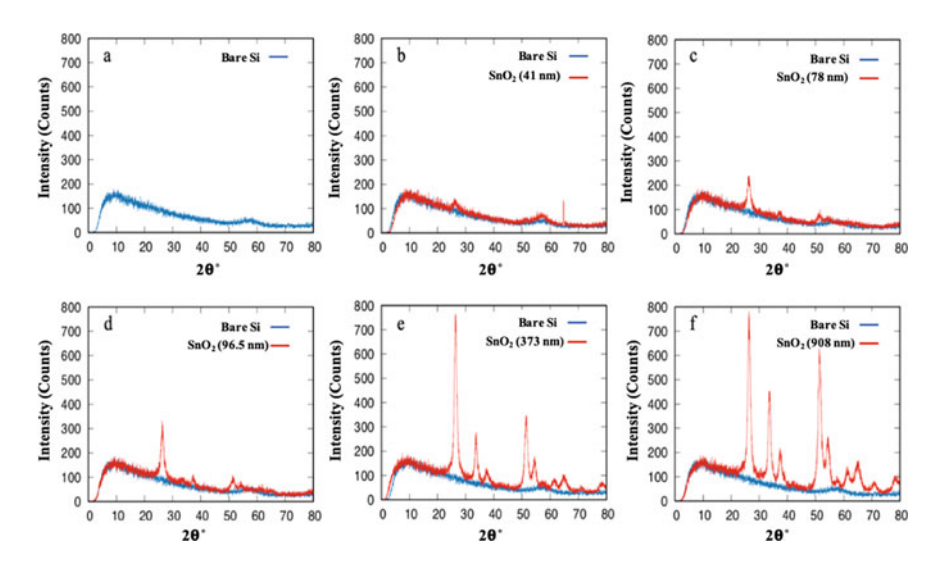


Fig. 14 XRD spectra of SnO_2 thin films on Si substrate: **a** bare double polished silicon wafer substrate, **b** comparison of silicon substrate with film of 41 nm thickness of SnO_2 , **c** silicon substrate with 78 nm SnO_2 film thickness, **d** silicon substrate with 96.5 nm SnO_2 thickness, **e** silicon substrate with 373 nm SnO_2 film thickness, **f** silicon substrate with 908 nm SnO_2 film thickness

the (110) orientation. As the thickness increases to 78 nm, another feature appears around 37.1°, which could be associated with the (200) index, along with the peak 51.36°, which corresponds to the (211) index. When the thickness of the tin dioxide film is 96.5 nm, the three previously mentioned peaks become more pronounced. With a thickness of 373 nm, the 33.64° with (101) index appears, along with other features that were not visible with thinner films.

In addition to the silicon substrate, XRD spectra were also taken for the tin dioxide films on quartz substrate, with the same thicknesses as on the Si substrate, starting from 41 nm and ending with 908 nm. Figure 15 shows the X-ray diffraction spectra of the SnO2 films in the range of $2\theta=0$ –80°. The data of bare quartz show a very broad peak at around 21.62°, and the broadening starts from $2\theta=10$ –35° approximately. The lowest ratios of tin dioxide thickness, namely 41 nm, 78 nm, and 96.5 nm, show no evidence of SnO2 structural peaks. The features of tin dioxide start to appear (i.e., 26.36° (110), 33.92° (101), 51.5° (211)) with the 373 nm thickness film, and become stronger and more pronounced with the 908 nm ratio with values (26.19°, 33.74°, 51.5°). It shows more of the amorphous behaviour due to the smaller size of the particles formed in the film in comparison with SnO2 on the Si substrate samples. From these data, we were able to calculate the crystallite size (D) using the Deybe-Scherrer formula in Eq. (5), as used by Agrahari et al. [1] and Henry et al. [23]:

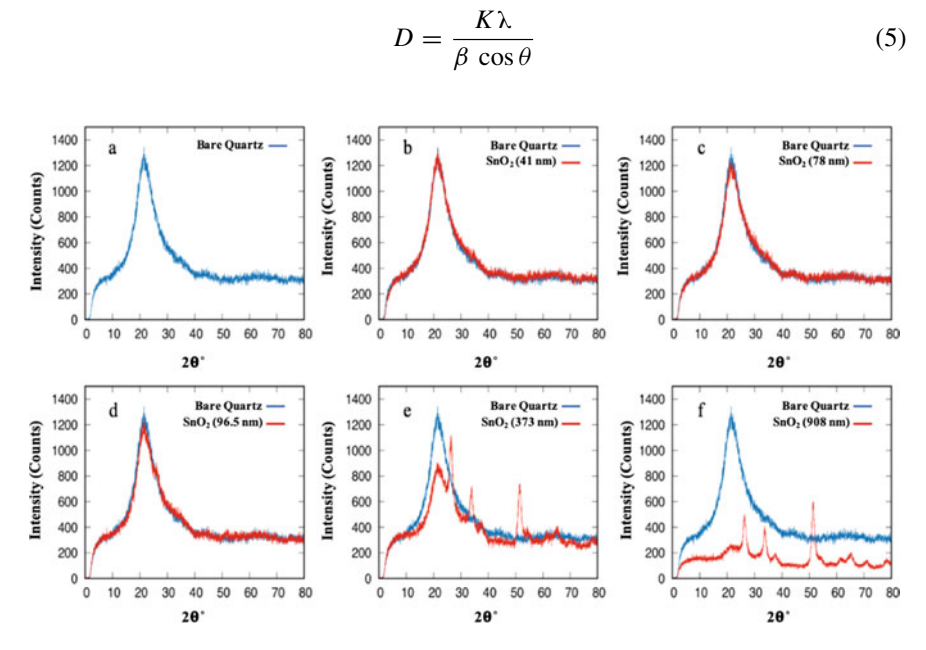


Fig. 15 XRD spectra of SnO₂ thin films on UV-Quartz substrate: **a** bare UV-Quartz substrate, **b** comparison of the Quartz substrate with film of 41 nm thickness of SnO₂, **c** Quartz substrate with 78 nm SnO₂ film thickness, **d** Quartz substrate with 96.5 nm SnO₂ thickness, **e** Quartz substrate with 373 nm SnO₂ film thickness, **f** Quartz substrate with 908 nm SnO₂ film thickness

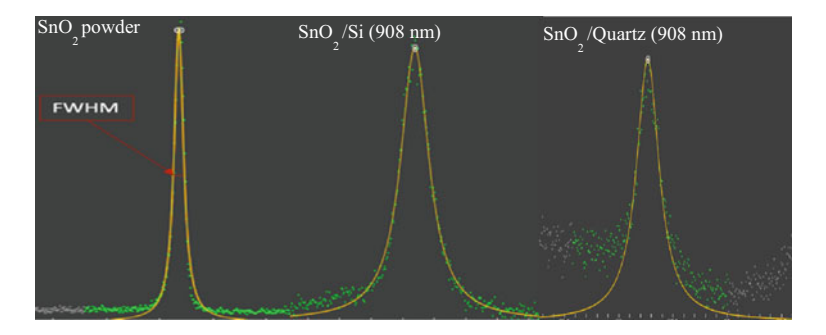


Fig. 16 Lorantzian fit for the first peak (110) orientation for SnO₂ samples

Table 2 Crystallite size (D) and interplanar distance (d) for SnO₂ powder and the most intense peak of SnO₂ with 908 nm thickness

Samples	Crystallite size D (nm)	Interplanar distance d (Å)
SnO ₂ powder	19.044	3.380
SnO ₂ /Si (908 nm)	7.367	3.375
SnO ₂ /Quartz (908 nm)	6.341	3.382

where K is a shape factor, typically K=0.89 for crystalline spherical solids with a cubic unit cell [18], λ is the wavelength, β is the broadening at half maximum (FWHM) in radians, θ is the Bragg's angle in radians. The most intense peak with a value of $2\theta=26.78^{\circ}$ was fitted by using a Cauchy-Lorentz distribution. The FWHM of the first peak was obtained using the Fityk software, as illustrated in Fig. 16.

The interplanar distance was calculated using Bragg's Law given by Eq. (6), obtained by rearranging Eq. (3):

$$d = \frac{\lambda}{2\sin\theta} \tag{6}$$

The results of both calculations are summarized in Table 3. As shown in Table 2, the crystallite size is smaller for the films than the powder. This is due to the amorphous behavior of the film with higher β values, whereas the interplanar distance has remained almost the same due to the choice of the first peak (110) orientation.

3.3 Scanning Electron Microscopy (SEM) of SnO₂

Images of different tin oxide samples were collected at various locations of the samples using the Phenom Pure Scanning Electron Microscope with magnification

ranging between 80x to 65,000x. In addition, the Phenom XL Desktop Scanning Electron Microscope was used with electron-optical magnification that ranged between 80x to 100,000x. The SEM images of the powdered sample with the Phenome pure SEM at 2 μ m magnification is shown in Fig. 17a, which can be utilized to pick one grain of the SnO_2 particle, and by using the Gwyddion software we can show a 3-dimensional view of the SEM image, as in Fig. 17b.

An average of 4 different spots of the powdered sample was obtained and has been summarized in Table 3. The $Z_{\rm Average}$ can be interpreted as an approximate height of an aggregate of nanoparticles beneath each spot of the SnO_2 sample studied. Also, we obtained the cross-section of the SnO_2 films on Si at 8 μ m magnification, which validated the approximate thickness of each sample (as shown in Fig. 18).

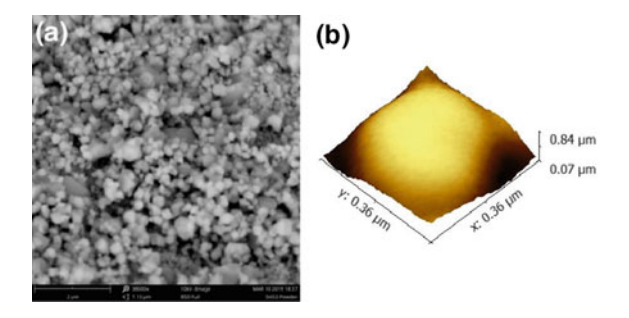


Fig. 17 a SEM image of SnO_2 powder at 2 μm magnification, b 3D view of SEM image of SnO_2 powder of single grain

Table 3 Averaged dimensions of 4 different spots at 2 μm magnification

Element	X _{Average} (μm)	Y _{Average} (μm)	Z _{Average} (μm)
SnO ₂ powder	0.49	0.51	0.75

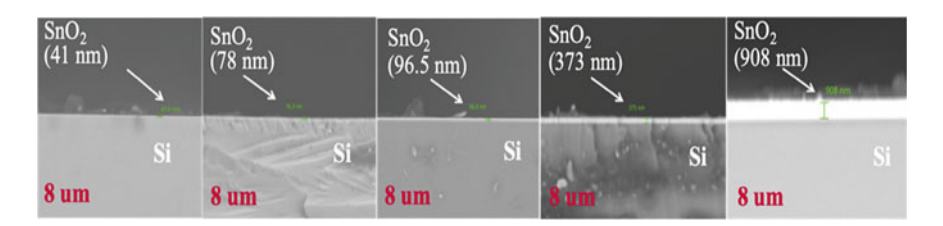


Fig. 18 Cross-sectional images of SnO₂/Si for various thicknesses

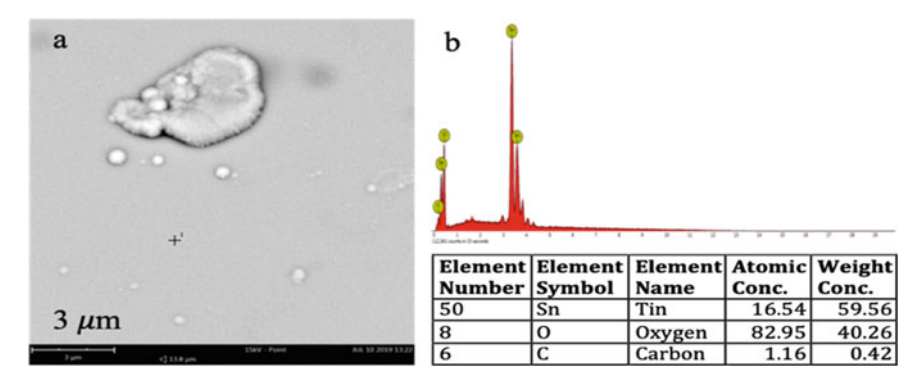


Fig. 19 SEM of SnO_2 on Si with 908 nm thickness at 3 μ m magnification (a). Corresponding EDS spectrum and composition data with accompanying tabulation of precise concentrations (b)

An arbitrary spot on the SnO₂ (908 nm) film on Si was analyzed at 3 μ m resolution with the Energy Dispersive X-Ray Spectroscopy (EDS) with the Phenom XL, which allowed analysis of the chemical composition of the film samples, as illustrated in Fig. 19.

The EDS analysis shows the atomic concentration and the weight concentration of SnO₂ to be 16.54 and 59.56, respectively, in comparison to the other elements in the Si sample. The EDS spectrum represents a plot of X-ray versus Energy in keV. The peaks represent a variety of elements in the sample [48].

3.4 FTIR Spectroscopy of SnO₂

We used the Thermo Scientific[™] Nicolet[™] iS50 FTIR Spectrometer, in order to determine the IR -active vibration modes for all tin dioxide samples studied. The ATR technique with diamond crystal was used to collect the Mid-IR spectra in the wavenumber range (400–4500 cm⁻¹). A Smart iTR[™] Attenuated Total Reflection (ATR) sampling accessory was used. The spectra were gained after collecting the background spectra and subtracting it from our sample spectra. Figure 20 shows the characterizing bands of pure SnO₂ powder in the range (400–800 cm⁻¹) [26] via peaks 467.36 cm⁻¹ (Sn–O stretching vibration) and 569.37 cm⁻¹ (Sn–O–Sn asymmetric vibration), in comparison to Sn–O around 530 cm⁻¹ [29, 32] and Sn–O–Sn around 600 cm⁻¹ [2].

The FT-IR spectra taken for all the silicon samples are shown in Fig. 21. At the lowest thicknesses, there is similar behavior to the silicon substrate results, with peaks at $1107.36 \, \text{cm}^{-1}$ (the Si-O₂ vibration band), and the $610.72 \, \text{cm}^{-1}$ feature due to lattice phonon absorption in agreement with Hava et al. [21].

The spectra for the 78 and 96.5 nm tin dioxide films exhibit peaks in the range (400–1150 cm⁻¹). The higher thickness SnO₂ films (373 nm and 908 nm) show

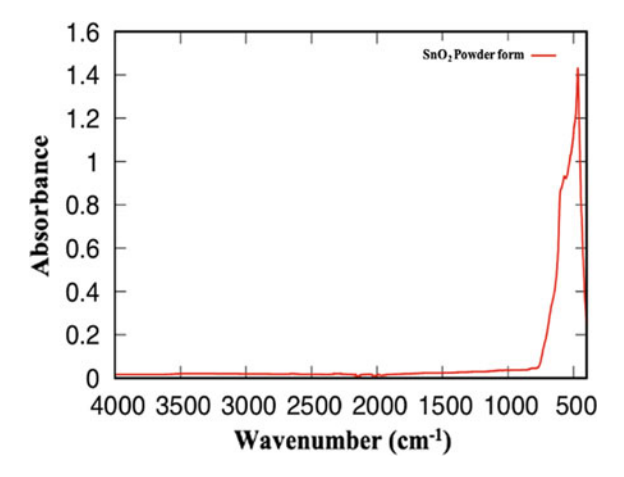


Fig. 20 FTIR spectrum of SnO₂ powder

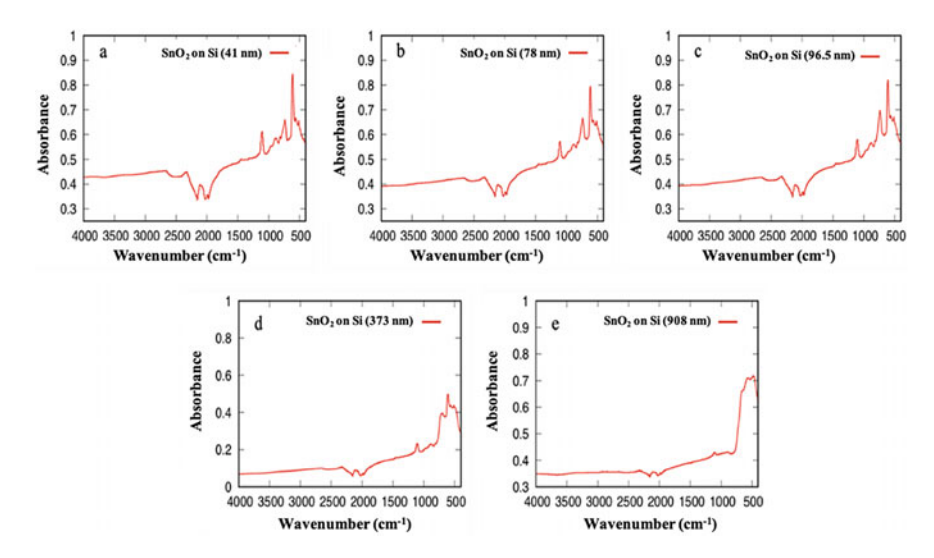


Fig. 21 FT-IR spectra of SnO_2 film on Si substrate: SnO_2 film thickness of 41 nm (a), 78 nm (b), 96.5 nm (c), 373 nm (d), 908 nm (e)

features of Si that start to disappear in the range (400–700 cm⁻¹). New features begin to appear in the 373 nm film thickness, with peaks around 692.44 cm⁻¹ and 565.57 cm⁻¹ that relate to the Sn–O stretching and Sn–O–Sn asymmetric vibrations, respectively [18].

The IR spectra for the SnO₂ thin films on quartz were collected to compare the results from different film thicknesses. Figure 22 shows all of the FT-IR data for bare quartz, indicating features that appear at 782.44 and 989.96 cm⁻¹, which represent

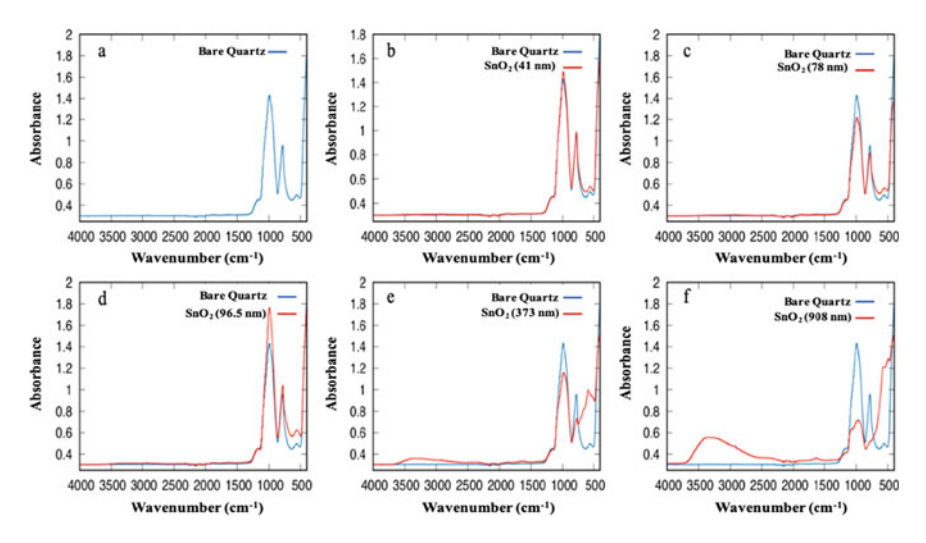


Fig. 22 FT-IR spectra of SnO₂ film on UV-Quartz substrate: Bare Quartz (a), SnO₂ film thickness of 41 nm (b), 78 nm (c), 96.5 nm (d), 373 nm (e), 908 nm (f)

the symmetric stretching of Si–O–Si, and symmetric and asymmetric stretching of Si–OH, similar to the spectra of silica-PLL [44]. There is no evidence of SnO₂ bands in the thinner films up through 96.5 nm thickness, where the only difference is that the baseline is higher in comparison to the two higher thickness films. When the thickness increases to 373 nm, the peak at 782.44 cm⁻¹ shifts to 776.68 cm⁻¹, together with an emergent peak at 589.64 cm⁻¹. Another feature around 406.17 cm⁻¹ starts to appear, which corresponds to the Sn–O vibration. Also, a peak due to the O–H bond appears around 3348.26 cm⁻¹. The highest thickness of 908 nm shows that the peak at 776.68 cm⁻¹ has vanished and instead we have peaks around 494.21 cm⁻¹ and 427.79 cm⁻¹, which are characteristic of SnO₂. Furthermore, the O–H bond becomes broader at the center of 3348.55 cm⁻¹, which may correspond to the presence of moisture in the thicker films. According to Dieguez et al., [14], when the crystal size is decreased, the IR spectra are modified due to the interaction between the particles and the electromagnetic radiation depending on the size, shape, and state of aggregation of the crystal.

3.5 Bandgap Energy Calculation for SnO₂

When UV-VIS light impinges on a crystalline solid, a portion (T) is transmitted through the surface of the sample, while some (R) is reflected at the surface, and the rest (A) is absorbed by the solid sample. The absorption pattern of the spectrum demonstrates the band structure of the sample, the energy gap between the lowest conduction band (CB) and the highest valence band (VB), and the nature of the

Table 4 Bandgap calculation for different thicknesses of SnO₂ films on Quartz

Thickness (nm)	Bandgap energy (eV)
78	3.458
96.5	3.383
373	3.562
908	3.519

transition, whether it is direct, indirect, forbidden, or allowed [11]. Using these principles, the UV-VIS transmission data taken with a Shimadzu UV-2600 UV-VIS Spectrophotometer allowed the calculation of the energy bandgap for the specified thicknesses of the SnO₂ films on Quartz as shown in Table 4.

The theoretical formulation to determine the band gap for the semiconductor material is given by Eq. (7):

$$\alpha E_p = k \left(E_p - E_g \right)^{1/2} \tag{7}$$

where α is the absorption coefficient, the k is a constant, and E_g is the band gap energy, and E_p is the discrete photon energy that was calculated using Eq. (8):

$$E_p = hv (8)$$

where h is Planck's constant and ν is the frequency of the light. The absorption coefficient α is calculated for the tin dioxide films as the absorbance divided by the thickness of the film. Ultimately, we used a classical Tauc plot to approximate the band gap energy E_g by plotting $\alpha^2 E_p^2$ against E_p . The x-intercept of this line represents the bandgap energy. A python script was written to optimize this process and has been included in the Appendix. The outputs of this script are shown in Fig. 23a–d and Table 5. As the film gets thicker the amount of noise in the absorbance spectra increases as exhibited by the E_p and $\alpha^2 E_p^2$ relationship in the plots, with a noticeable increase in the band gap value.

In an attempt to reduce the noise in the absorption spectra of SnO_2 on UV-Quartz, an annealing process was applied to the two thicker films. The 373 and 908 nm films were annealed up to 360 °C for 15 min. The results of annealing the tin dioxide films in comparison with the unannealed films are illustrated in Fig. 24. The band gap calculation for the annealed sample appeared to be enhanced over that of the as deposited SnO_2 films. The band gap of 373 nm was at 3.562 eV as deposited and after annealing it increased to 3.580 eV. For the 908 nm thickness the as deposited band gap was 3.519 nm and after annealing it increased to 3.552 eV.

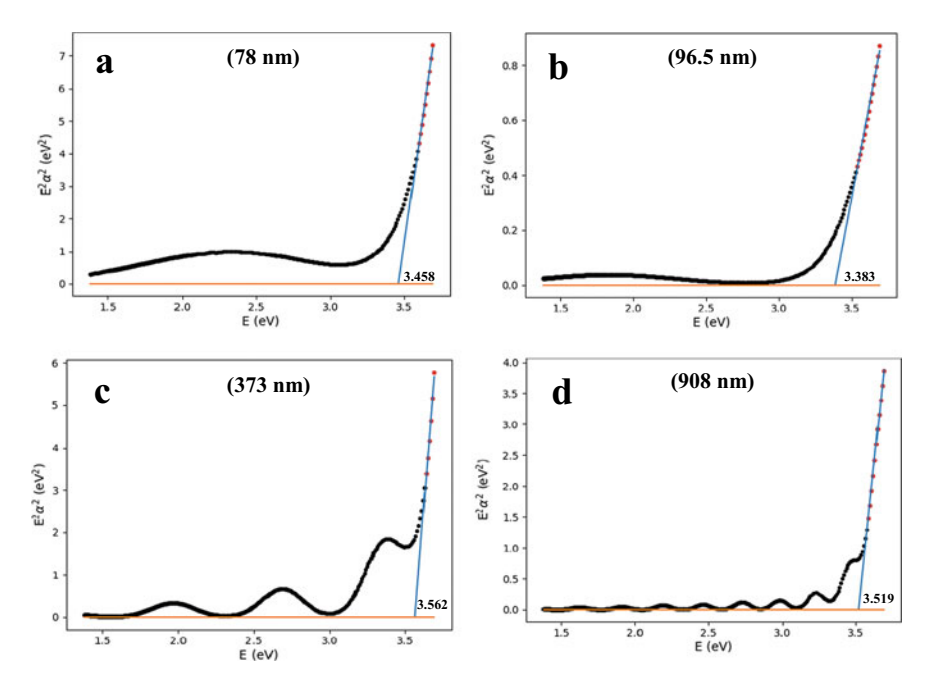


Fig. 23 Bandgap calculation for different thicknesses of SnO₂ films on UV-Quartz: (a) 78 nm, (b) 96.5 nm, (c) 373 nm, (d) 908 nm

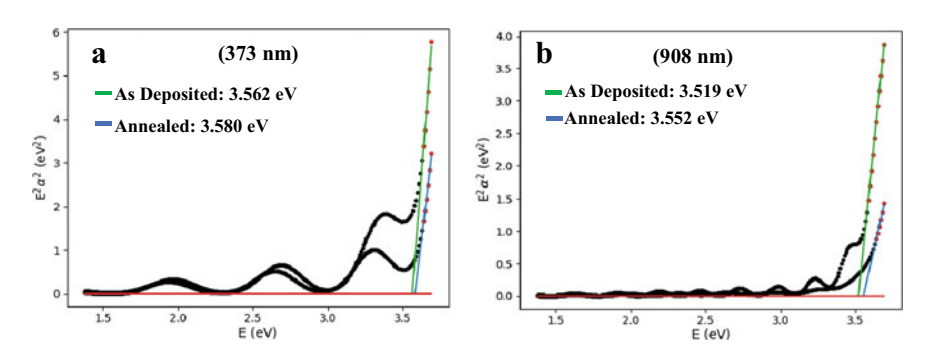


Fig. 24 Bandgap calculation of SnO_2 on UV-Quartz as deposited (green) and annealed (blue) of two thicker films: (a) 373 nm, (b) 908 nm

4 Composites with Metal Oxides

4.1 Carbon-Based Composites

Among all tin dioxide composites, carbon-based materials stand out due to their superior electrochemical properties. A study done by Paek et al. [40] showed improvements in both the reversible capacity and cyclic performance when combining graphene nanosheets (GNS) with the SnO₂ anode material in Lithium-ion batteries. The graphene nanosheet was prepared by the method of chemical reduction of exfoliated oxidized graphite materials. The SnO₂ was prepared by controlled SnCl₄ hydrolysis with NaOH. One-dimensional SnO₂ n-type semiconductor coated with a single-wall carbon nanotube (SWCNT) was used to increase the gas sensitivity for gas-sensing applications, in contrast to only p-type semiconducting SWCNT [25]. The hybrid of SnO₂ and SWCNT showed improved sensitivity, especially towards the detection of nitrogen dioxide (NO₂), as reported by Wei et al. [54]. A gas sensor based on hybrid SnO₂/SWNTs has been designed to sense O₃ and NH₃ and has shown enhancement in detecting O₃ and NH₃ in comparison to pure SWCNTs layers at room temperature [20]. Moreover, n-type multi-walled nanotube (MWNT) fiber composites with SnO₂ prepared by electrospinning and calcined in air at 500 °C have been able to detect carbon monoxide (CO) at room temperature at 50 ppm concentration, whereas pure SnO₂ nanofibers were found to be not sensitive under these conditions up to 500 ppm [57].

4.2 Polymer Composites

Several composites have been produced by using Polyurethanes (PUs), which are an important class of polymer materials, because of their chemical, mechanical, and physical properties. There are many forms of PU: rigid and flexible foams, chemical resistant coatings used as sealants, adhesives, and elastomers. The foam form of PU is favored due to its desirable features, such as enhanced moisture resistance and good sound damping. There are some limitations with the PU foams, such as low mechanical properties and poor thermal stability. The thermal stability of Polyurethanes was improved with the addition of tin dioxide nanoparticles at different densities of PU foam [17]. Also, addition of ceramic powders of tin dioxide to a system of Nafion-based polymer membranes was noted to enhance their chemical and physical properties and led to increased water affinity, higher modulus storage of membrane composites, and furthered polymer ionic channel organizations [46].

5 Engineering Applications of Metal Oxides

5.1 Gas Sensors

Gas sensors based on metal oxides have seen a resurgence in recent years [13]. Tin dioxide in different forms and shapes has been used in a variety of safety, industrial and health applications. It has been used in the production of cost-effective and reliable gas sensors (SMOX) [13] that are relatively simple to fabricate and use [55]. The mechanism of operation of a gas sensor is based on the changes in conductivity of these materials through adsorption and desorption of gases, such as oxygen, on the metal oxide surface. The surface of the metal oxide reacts with the detected gases. The absorbed oxygen gets captured at the grain limit trap sites, and thereby the barrier of the grain boundary potential increases, which leads to an increase in the material resistivity [33]. As a result of this process, the electrical resistivity of a semiconductor metal oxide becomes responsive to any impurities that might be present on its surface or within its volume [22]. The first generation of merchant sensor devices was manufactured in 1968 in Japan by Taguchi Gas Sensor (TGS). They used SnO₂ thick films as their sensing material to detect flammable gases [6]. Certain physical and chemical properties for the gas-sensing materials need to be met in order to have an ideal gas sensor. For example, the sensing material should have high long-term stability over a wide temperature range, with fast and high response to the target gas and low response to ambient gases and humidity that exist in the atmosphere, high selectivity, and cost-effective machinery. However, existing sensors have their pros and cons. Metals, metal oxides, and polymers are frequently employed materials in gas-sensing applications. Metal oxides have shown better sensitivity performance as compared to metals and polymers and exhibit good stability at high temperatures, while metals showed fair stability and polymers had unsatisfactory stability as gas sensors. Metals on the other hand are the most costeffective sensing materials, in comparison to metal oxides (fair cost) and polymers (intermediate cost). Although metal oxides perform efficiently with almost all the properties mentioned earlier, their selectivity could be enhanced. Consequently, the metal oxides have been tailored to detect diverse gases using functionalized and composites of SnO₂, as summarized in Table 6. Pure SnO₂ has been used by itself in a chemoresistor-based gas sensor in order to detect a variety of reducing gases, such as hydrogen (H₂), carbon monoxide (CO) carbon dioxide (CO₂), and methane (CH₄) [29]. The sensitivity of gas sensors based on metal oxide semiconductors is affected by the film thickness. Reducing the size of SnO2 particles to a scale of nanometer dimensions and thin films, results in an enhancement in responsiveness, down to the Debye length. The Debye length describes the space-charge size area next to the free carrier concentration surface [16]. Specifically, it has been found that by decreasing the crystallite size (D) of SnO₂ to a range of 5–32 nm the sensitivity towards certain gases, such as (CO), (H₂), and (i-C₄H₁₀), increases [56]. A separate study conducted by Hijazi et al. [24] showed good sensitivity and selectivity of pure SnO₂ and SnO₂ functionalized with 3-aminopropyltriethoxysilane (APTES)

Table 5 Compendium of pure and functionalized tin dioxide materials for detecting gases

Material	Detected gases	
a, b, cPure SnO ₂	CO, H ₂ , CH ₄ , i-C ₄ H ₁₀	
^d Functionalized APTES SnO ₂ with alkyl: C ₆ H ₁₁ ClO ester: C ₇ H ₁₁ ClO ₃ acid: C ₆ H ₈ Cl ₂ O ₂	NH ₃	

^aXu et al. [56]

labeled (SnO₂-APTES) toward ammonia (NH₃) gas in an aim to detect gases from exhaled breath to diagnose diseases. SnO₂-APTES was further functionalized with alkyl ($C_6H_{11}CIO$), acid ($C_6H_8Cl_2O_2$), and ester ($C_7H_{11}CIO_3$) groups. Both (SnO₂-APTES-acid) and (SnO₂-APTES-ester) have shown an increase in conductance (i.e. sensitivity) as compared to (SnO₂-APTES-alkyl) when exposed to 100 ppm of NH₃ gas; whereas pure SnO₂ and SnO₂-APTES have shown no change in conductance in the presence of ammonia gas. In addition, (SnO₂-APTES-acid) exhibited superior selectivity for NH₃ as compared to (SnO₂-APTES-ester), while pure SnO₂ works well for detecting carbon monoxide, hydrogen, methane and isobutane (see Table 5).

5.2 Lithium-Ion Batteries

Owing to their superior electrochemical properties, SnO₂-based materials exhibit high specific capacity and cost-effective ingredients. The SnO₂ anode has shown an increase in reversible discharge capacity of 782 mAh/g. However, the regular SnO₂ anode suffers from low cycling ability and cracks due to volume changes with cycling. By reducing the size of the SnO₂ particles, it is possible to increase the ratio of surface-to-volume and lower the change in volume during insertion and extraction of lithium [50]. For instance, nanoparticles of SnO₂ of size 3 nm have shown enhanced electrochemical properties, but with low lithium storage, in comparison to those of 4 nm and 8 nm particle sizes [27]. Song et al. have studied three higher particles sizes with $(SnO_2-I = 15 \text{ nm})$, $(SnO_2-II = 30 \text{ nm})$, and $(SnO_2-III = 70 \text{ nm})$, where SnO_2-I has shown stable electrochemical performance during different cycles. SnO₂–I also showed an improvement in discharge capacity after 30 cycles (i.e. charging and discharging 30 times) with capacity around 460 mAh/g, which means it holds 58.2% of its electrical capacity in comparison to SnO₂-II and SnO₂-III that hold 40.7% and 21.0%, respectively [50]. Also, SnO₂ nanowires were found to be a promising anode material due to their unique structural and electronic properties. However, there were limitations to the use of tin dioxide nanowire anodes in lithium-ion batteries, which was related to the deteriorative effects of catalysts [41]. The electrochemical properties of SnO₂ anode-based battery could be improved by performing appropriate

^bKorotcenkov et al. [29]

^cDu and George [16]

^dHijazi et al. [24]

nanostructure enhancements in chemical composition. Theoretically, the tin dioxide anode in lithium-ion batteries was found to be distinctive due to its high capacity [10]. A study conducted by Wang et al. [52] showed that the use of N-doped graphene-SnO $_2$ anodes in lithium-ion batteries resulted in higher capacity, as well as an increase in rate capability, and improved cycling stability performance. Such enhancements were directly related to the exceptional electronic conductivity and sandwich structure of the doped graphene that facilitated short-length transportation of the electrons and lithium ions.

5.3 Solar Cells

There has been an increasing amount of research relating to the enhancement of optical sensors, such as photodiodes, regarding their sensitivity to light in the ultraviolet (UV) region. SnO₂ nanoforms have been applied in dye-sensitized and polymerbased solar cells due to their large band gaps, thermal stabilization, low photocatalytic activity, elevation of electron mobility, and fine anti-reflection properties [37]. In addition, SnO₂ can be used as a coating that improves the sensitivity of traditional GaP and ZnSe based photodiodes in the UV spectral limit. The uncoated photodiodes reach their limit in the range 200-380 nm. Anti-reflection (AR) coating can be used to increase the absorbance of light and reduce the loss of photons. A SnO₂ nanosized layer acts as an optically transparent coating layer that allows the photodiode to detect light at shorter wavelengths. SnO₂ can also be employed as a transparent active electrode that functions in the wavelength range 350-1100 nm. The high transparency of SnO₂ comes from the large magnitude of the band gap energy (Eg ~ 3.6 eV). The structure of the SnO₂ layer leads to refraction that suits the formation of AR coatings. Adding a coating layer of SnO₂ with 54.4 nm thickness leads to a transmission coefficient of 9.6% at 435 nm. In one study, an SnO₂ sheet was used with two different photodiodes, one with zinc selenide (ZnSe) and the other with gallium phosphide (GaP). The AR coating of SnO₂ on ZnSe and GaP based photodiode showed an increase in sensitivity of about 10–15% [15]. The SnO₂ thin films prepared by a sol-gel method were also used in AR coating for solar cells. The sol-gel method created high purity films based on the hydrolysis and the polycondensation of metal-organic precursors. It also offered a nanoscale control of the film structure. The use of tin oxide (SnO₂)/silicon (Si) has been proposed for low-cost photovoltaic devices. The doping in SnO₂ has been used to reduce the sheet resistance and to increase the transparency of the thin film. The doped SnO₂ has proven to provide high optical clarity of the obtained films. Also, due to this layer, the device has excellent technical performance and high reliability, without large fabrication costs [34]. SnO₂ has also been exploited as an electron transfer material (ETM) (i.e. coating material) in perovskite solar cells. Organometallic halide perovskite (ABX₃) has been studied extensively in recent years due to its distinctive properties, such as large absorption coefficient and optimal band gap, which qualify it for absorbing light applications in photovoltaic cells. The SnO₂ nanomaterial is

featured with its high electron mobility ($0.8 \pm 0.14~\text{cm}^2/\text{V}$ s), in comparison with zinc oxide (ZnO) and titanium dioxide (TiO₂) with mobilities ($0.08 \pm 0.01~\text{cm}^2/\text{V}$ s) and ($0.1 \pm 0.03~\text{cm}^2/\text{V}$ s), respectively. SnO₂ has been prepared as an ETM in perovskite by a solution processing method in which the SnO₂ films were deposited from SnCl₂ solution of 0.1~M concentration by using water and ethanol as solvents. By using ethanol as a solvent, the coating material showed an enhancement in the UV/VIS absorption spectra by 8.38%, with enhanced incident photon-to-electron conversion efficiency (IPCE) and a circuit current density (J_{SC}) of $18.98~\text{mA}~\text{cm}^{-2}$ [37].

6 Conclusions and Future Research

We have characterized SnO₂ powder, SnO₂/Si and SnO₂/UV-Quartz films by using Raman, FT-IR, XRD, SEM, and UV-VIS spectroscopy techniques. We have demonstrated a red shift in the Raman spectra as the temperature increases from 30 to 170 °C in both A_{1g} and B_{2g} vibrational modes, while E_g exhibited little change. By using a 532 nm laser Raman excitation we were able to record the three Raman active modes for SnO₂ (908 nm thickness) film on quartz, which were difficult to view at Raman excitation wavelengths of 780 and 514 nm. We performed a visual characterization in three dimensions to obtain the morphology of SnO₂ powder (bulk form) and SnO₂ film on silicon substrate utilizing high resolution scanning electron microscopy. Additional trials for temperature-dependence are underway for SnO₂ film samples to study the effects of both decreasing and increasing temperatures. An approach utilizing the local-density approximation by using ab initio software has shown an agreement of phonon frequency relation with IR and Raman spectra [42]. Another approach followed by Lan et al. [31, 30] uses Molecular Dynamics (MD) simulation for the rutile structured TiO₂ to calculate the shifts and broadenings of anharmonic frequency phonon modes at different temperatures ranging between (100–1150 K) by using GULP software. Their MD simulation showed agreement of crystal structure (i.e. lattice parameters), Raman frequencies and thermal expansion with the experimental data. We are studying rutile structured SnO₂ using MD simulation at different temperatures integrated within the Large-scale Atomic/Molecular Massively Parallel Simulator (LAMMPS) software. High-level computations are in progress utilizing MD simulations to compare our experimental data with theoretical results, in order to gain a deeper insight into the effects of temperature on the phonon modes active in rutile tetragonal tin dioxide.

Acknowledgements Financial support from the National Science Foundation (REU Site in Physics at Howard University, NSF Award# PHY-1659224) is gratefully acknowledged. We also would like to acknowledge the assistance of the technical staff and the use of the X-ray diffraction and Raman instrumentation at the Thermo Fisher Scientific facilities in Lanham, MD, for some of the tin dioxide spectral measurements reported here.

Appendix

```
#Python code for calculating the energy bandgap for SnO2 from
UV-VIS Spectra
import csv
import numpy as np
import matplotlib.pyplot as plt
import easygui
import sys
\mathbf{x} = []
y = \prod
#Get Data from CSV file
string = easygui.fileopenbox(default = "D:\\D Docu-
ments\\REU Howard 19\\5 29 19") #this string should be changed
based on your directory
with open(string) as csvDataFile:
  csvReader = csv.reader(csvDataFile)
  for row in csvReader:
     x.append(row[0])
     y.append(row[1])
#this reads a CSV file where the first row is the Energy E, and the
second is E^2 * Alpha^2
#Alternatively, one can change the numbers on the rows above to
read different rows from the file
xx = np.array(x)
yy = np.array(y)
```

```
xx = [float(xx) for xx in xx]
yy = [float(yy) for yy in yy]
#Python Housekeeping
size = np.size(xx)
cut = -565
xx = xx[cut:]
yy = yy[cut:]
#This is where the zooming occurs, you can change this by adjusting
the number "cut"
#It looks at the last "cut" numbers of the array
E = xx
Ealphsq = yy
plt.plot(E, Ealphsq,'k.')
#Changing the variable names to something more intuitive, and here
I plot the data so I'm
not in the dark
for i in range(0,1-4):
  if abs(abs((Ealphsq[i] - Ealphsq[i+3])/(E[i]-E[i+3])) - sl) < tol*sl:
     line[k] = Ealphsq[i]
     k = k+1
  else:
     sl = np.Infinity
#This loop finds the data we want in the line at the end
```

if k < 1:

```
print('I died, graph does not terminate in line')
  sys.exit #If you didn't zoom right you'll see this printed, or if you
pick bad data
v = np.zeros(k)
Evec = np.zeros(k)
for i in range(k):
  v[k-i-1] = line[i]
  Evec[i] = E[k-i-1]
plt.plot(Evec,v,'r.')
#plot the points we have chosen to be a part of our line
A = np.column stack((np.transpose(Evec), np.ones(k)))
AtA = np.matmul(np.transpose(A), A)
v.shape = (k,1)
Atv = np.matmul(np.transpose(A),v)
b = np.linalg.solve(AtA,Atv)
#Normal equations for line of best fit
incpt = -b[1]/b[0]
print('x intercept occurs at Eg = ')
print(incpt)
x = np.linspace(E[0],incpt,150)
y = x*b[0] + b[1]
```

```
plt.plot(x,y)
plt.plot(xx,np.zeros(np.size(xx)))
plt.title('E$_g$ = ' + str(incpt))
plt.xlabel("E (eV)")
plt.ylabel('E$^2$$ \\alpha ^2$ (eV$^2$)')
#print x-intercept
```

References

- Agrahari, V., Mathpal, M.C., Kumar, S., Kumar, M., Agarwal, A.: Cr modified Raman, optical band gap and magnetic properties of SnO₂ nanoparticles. J. Mater. Sci.: Mater. Electron. 27, 6020–6029 (2016). https://doi.org/10.1007/s10854-016-4525-2
- Ansari, S.G., Fouad, H., Shin, H.S., Ansari, Z.A.: Electrochemical enzyme-less urea sensor based on nano-tin oxide synthesized by hydrothermal technique. Chem. Biol. Interact. 242, 45–49 (2015)
- Armstrong, P., Knieke, C., Mackovic, M., Frank, G., Hartmaier, A., Goken, M., Peukert, W.: Microstructural evolution during deformation of tin dioxide nanoparticles in a comminution process. Acta Materialia 57(10), 3060–3071 (2009)
- 4. Batzill, M., Diebold, U.: The surface and materials science of tin oxide. Prog. Surf. Sci. 79, 47–154 (2005). Reprinted from Progress in Surface Science, Vol 79, Issues 24, Matthias Batzill and Ulrike Diebold, The surface and materials science of tin oxide, Page 70, Copyright (2019), with permission from Elsevier
- Berthomieu, C., Hienerwadel, R.: Fourier transform infrared (FTIR) spectroscopy. Photosynth. Res. 101(2–3), 157–170 (2009)
- Briand, D., Courbat, J.: Micromachined semiconductor gas sensors. Semicond. Gas Sens. 220–260 (2013). https://doi.org/10.1533/9780857098665.2.220
- Bumbrah, G.S., Sharma, R.M.: Raman spectroscopy—basic principle, instrumentation and selected applications for the characterization of drugs of abuse. Egypt. J. Forensic Sci. 6(3), 209–215 (2016)
- Casimir, D., Ahmed, I., Garcia-Sanchez, R., Misra, P., Diaz, F.: Raman spectroscopy of graphitic nanomaterials. In: Raman Spectroscopy. Gustavo M. do Nascimento (ed.) IntechOpen. https:// doi.org/10.5772/intechopen.72769 (2017)
- Cañas-Carrell, J.E., Li, S., Parra, A.M., Shrestha, B.: Metal oxide nanomaterials: health and environmental effects. In: Health and Environmental Safety of Nanomaterials, pp. 200–221. Woodhead Publishing (2014)
- Chen, J.S., Lou, X.W.: SnO₂-based nanomaterials: synthesis and application in lithium-ion batteries. Small 9(11), 1877–1893 (2013)
- 11. Chowdhury, F.R., Choudhury, S., Hasan, F., Begum, T.: Optical properties of undoped and indium-doped tin oxide thin films. J. Bangladesh Acad. Sci. 35(1), 99–111 (2011)
- Das, S., Jayaraman, V.: SnO₂: a comprehensive review on structures and gas sensors. Prog. Mater. Sci. 66, 112–255 (2014)
- Degler, D.: Spectroscopic insights in the gas detection mechanism of tin dioxide-based gas sensors. Doctoral dissertation, Eberhard Karls Universität Tübingen (2017)

14. Dieguez, A., Romano-Rodriguez, A., Vila, A., Morante, J.R.: The complete Raman spectrum of nanometric SnO2 particles. J. Appl. Phys. **90**(3), 1550–1557 (2001)

- Dobrovolskiy, Y.G., Perevertailo, V.L., Shabashkevich, B.G.: Anti-reflection coatings based on SnO₂, SiO₂, Si₃N₄ films for photodiodes operating in ultraviolet and visible spectral ranges. Semicond. Phys. Quantum Electron. Optoelectron. 14(3), 298–301 (2011)
- Du, X., George, S.M.: Thickness dependence of sensor response for CO gas sensing by tin oxide films grown using atomic layer deposition. Sens. Actuators B: Chem. 135(1), 152–160 (2008)
- 17. Esmailzadeh, M., Manesh, H.D., Zebarjad, S.M.: Role of SnO₂ nanoparticles on mechanical and thermal properties of flexible polyurethane foam nanocomposite. J. Porous Mater. **23**(5), 1381–1388 (2016)
- Ferreira, C.S., Santos, P.L., Bonacin, J.A., Passos, R.R., Pocrifka, L.A.: Rice husk reuse in the preparation of SnO₂/SiO₂ nanocomposite. Mater. Res. 18(3), 639–643 (2015). https://doi.org/ 10.1590/1516-1439.009015. Retrieved from SciELO—Scientific Electronic Library Online Publishing with open access source
- Fierro, J.L.: Metal Oxides Chemistry and Applications, pp. 178–181. Taylor & Francis Group, Boca Raton, FL (2006). ISBN: 978-0-8247-2371-2
- Ghaddab, B., Berger, F., Sanchez, J.B., Mavon, C.: Detection of O₃ and NH₃ using tin dioxide/carbon nanotubes-based sensors: influence of carbon nanotubes properties onto sensor's sensitivity. Procedia Eng. 5, 115–118 (2010)
- Hava, S., Ivri, J., Auslender, M.: Wavenumber-modulated patterns of transmission through one-and two-dimensional gratings on a silicon substrate. J. Opt. A: Pure Appl. Opt. 3(6), S190 (2001)
- 22. Henrich, V.E., Cox, P.A.: The Surface Science of Metal Oxides. Cambridge University Press (1996)
- Henry, J., Mohanraj, K., Sivakumar, G., Umamaheswari, S.: Electrochemical and fluorescence properties of SnO₂ thin films and its antibacterial activity. Spectrochim. Acta Part A: Mol. Biomol. Spectrosc. 143, 172–178 (2015)
- 24. Hijazi, M., Stambouli, V., Rieu, M., Tournier, G., Pijolat, C., Viricelle, J.P.: Sensitive and selective ammonia gas sensor based on molecularly modified SnO₂. In: Multidisciplinary Digital Publishing Institute Proceedings, vol. 1, no. 4, p. 399 (2017)
- Hoa, N.D., Quy, N.V., Wei, L., An, M., Song, H., Kang, Y., Kim, D.: One-dimensional tinoxide-coated single-wall carbon nanotubes for gas sensor applications. J. Korean Phys. Soc. 54, 1893 (2009)
- Juliasih, N., Buchari, Noviandri, I.: Application of SnO₂ nanoparticle as sulfide gas sensor using UV/VIS/NIR spectrophotometer. IOP Conf. Ser.: Mater. Sci. Eng. 188, 012025 (2017). https://doi.org/10.1088/1757-899x/188/1/012025
- Kim, C., Noh M., Choi, M., Choi, J., Park, B.: Critical size of a nano SnO₂ electrode for Li-secondary battery. Chem. Mater. 17, 3297–3301 (2005)
- 28. Konijnendijk, W.L., Stevels, J.M.: The structure of borosilicate glasses studied by Raman scattering. J. Non-Cryst. Solids **20**(2), 193–224 (1976)
- Korotcenkov, G., Brinzari, V., Ham, M.H.: Materials acceptable for gas sensor design: advantages and limitations. In: Key Engineering Materials, vol. 780, pp. 80–89. Trans Tech Publications Ltd. (2018)
- 30. Lan, T., Tang, X., Fultz, B.: Phonon anharmonicity of rutile TiO₂ studied by Raman spectrometry and molecular dynamics simulations. Phys. Rev. B **85**(9), 094305 (2012)
- Lan, T., Li, C., Fultz, B.: Phonon anharmonicity of rutile SnO₂ studied by Raman spectrometry and first principles calculations of the kinematics of phonon-phonon interactions. Phys. Rev. B 86(13) (2012). https://doi.org/10.1103/PhysRevB.86.134302
- 32. Mahadik, D.B., Lee, Y.K., Park, C.S., Chung, H.Y., Hong, M.H., Han, W., Park, H.H.: Effect of water ethanol solvents mixture on textural and gas sensing properties of tin oxide prepared using epoxide-assisted sol–gel process and dried at ambient pressure. Solid State Sci. **50**, 1–8 (2015)

- 33. Majumder, S.: Synthesis and characterization of SnO₂ films obtained by a wet chemical process. Mater. Sci. **27**(2) (2009). ISSN: 0137-1339
- 34. Manea, E., Budianu, E., Purica, M., Podaru, C., Popescu, A., Cernica, I., Parvulescu, C.C.: SnO₂ thin films prepared by sol gel method for 'Honeycomb' textured silicon solar cells. Romanian J. Inf. Sci. Technol. **10**(1), 25–33 (2007)
- 35. Mathew, X., Enriquez, J.P., Mejia-Garcia, C., Contreras-Puente, G., Cortes-Jacome, M.A., Toledo Antonio, J.A., Punnoose, A.: Structural modifications of SnO₂ due to the incorporation of Fe into the lattice. J. Appl. Phys. **100**(7), 073907 (2006)
- 36. Mukhopadhyay, A.: Measurement of Magnetic Hysteresis Loops in Continuous and Patterned Ferromagnetic Nanostructures by Static Magneto-Optical Kerr Effect Magnetometer. Satyendra Nath Bose National Centre for Basic Sciences, Guwahati (2015)
- 37. Murugadoss, G., Kanda, H., Tanaka, S., Nishino, H., Ito, S., Imahori, H., Umeyama, T.: An efficient electron transport material of tin oxide for planar structure perovskite solar cells. J. Power Sources **307**, 891–897 (2016)
- 38. Nasdala, L., Smith, D.C., Kaindl, R., Ziemann, M.A.: Raman spectroscopy: analytical perspectives in mineralogical research. Spectrosc. Methods Mineral. **6**, 281–343 (2004)
- 39. Oviedo, J., Gillan, M.J.: Energetics and structure of stoichiometric SnO2 surfaces studied by first-principles calculations. Surf. Sci. **463**(2), 93–101 (2000)
- Paek, S.M., Yoo, E., Honma, I.: Enhanced cyclic performance and lithium storage capacity of SnO₂/graphene nanoporous electrodes with three-dimensionally delaminated flexible structure. Nano Lett. 9(1), 72–75 (2008)
- 41. Park, M.S., Wang, G.X., Kang, Y.M., Wexler, D., Dou, S.X., Liu, H.K.: Preparation and electrochemical properties of SnO2 nanowires for application in lithium-ion batteries. Angew. Chem. Int. Ed. 46(5), 750–753 (2007)
- 42. Parlinski, K., Kawazoe, Y.: Ab initio study of phonons in the rutile structure of SnO₂ under pressure. Eur. Phys. J. B Condens. Matter Complex Syst. **13**(4), 679–683 (2000)
- Patil, G.E., Kajale, D.D., Gaikwad, V.B., Jain, G.H.: Preparation and characterization of SnO₂ nanoparticles by hydrothermal route. Int. Nano Lett. 2(1) (2012). https://doi.org/10.1186/2228-5326-2-17
- 44. Patwardhan, S.V., Maheshwari, R., Mukherjee, N., Kiick, K.L., Clarson, S.J.: Conformation and assembly of polypeptide scaffolds in templating the synthesis of silica: an example of a polylysine macromolecular "switch". Biomacromolecules 7(2), 491–497 (2006)
- 45. Peercy, P., Morosin, B.: Pressure and temperature dependences of the Raman-active phonons in SnO₂. Phys. Rev. B **7**(6), 2779–2786 (1973). https://doi.org/10.1103/PhysRevB.7.2779
- Scipioni, R., Gazzoli, D., Teocoli, F., Palumbo, O., Paolone, A., Ibris, N., Navarra, M.: Preparation and characterization of nanocomposite polymer membranes containing functionalized SnO₂ additives. Membranes 4(1), 123–142 (2014)
- 47. Sergent, N., Epifani, M., Pagnier, T.: In situ Raman spectroscopy study of NO₂ adsorption onto nanocrystalline tin (IV) oxide. J. Raman Spectrosc. **37**, 1272–1277 (2006)
- 48. Severin, K.P.: Energy Dispersive Spectrometry of Common Rock Forming Minerals, p. 19. Kluwer Academic, Dordrecht, The Netherlands (2004)
- 49. Sharma, R., Bisen, D.P., Shukla, U., Sharma, B.G.: X-ray diffraction: a powerful method of characterizing nanomaterials. Recent Res. Sci. Technol. 4(8) (2012). Recreated from Recent Research in Science and Technology Publishing with open access source
- 50. Song, H., Li, X., Cui, Y., Xiong, D., Wang, Y., Zeng, J., Sun, X.: Controllable lithium storage performance of tin oxide anodes with various particle sizes. Int. J. Hydrog. Energy **40**(41), 14314–14321 (2015)
- 51. Su, H.-W., Chen, W.-C.: High refractive index polyimide–nanocrystalline-titania hybrid optical materials. J. Mater. Chem. **18**(10), 1139 (2008). https://doi.org/10.1039/b717069f
- 52. Wang, X., Cao, X., Bourgeois, L., Guan, H., Chen, S., Zhong, Y., Bando, Y.: N-doped graphene-SnO₂ sandwich paper for high-performance lithium-ion batteries. Adv. Funct. Mater. **22**(13), 2682–2690 (2012)
- Wang, F., Zhou, X., Zhou, J., Sham, T.K., Ding, Z.: Observation of single tin dioxide nanoribbons by confocal Raman microspectroscopy. J. Phys. Chem. C 111(51), 18839–18843 (2007)

54. Wei, B.Y., Hsu, M.C., Su, P.G., Lin, H.M., Wu, R.J., Lai, H.J.: A novel SnO₂ gas sensor doped with carbon nanotubes operating at room temperature. Sens. Actuators B: Chem. **101**(1–2), 81–89 (2004)

- 55. Wilson, R., Simion, C., Blackman, C., Carmalt, C., Stanoiu, A., Di Maggio, F., Covington, J.: The effect of film thickness on the gas sensing properties of ultra-thin TiO₂ films deposited by atomic layer deposition. Sensors **18**(3), 735 (2018)
- 56. Xu, C., Tamaki, J., Miura, N., Yamazoe, N.: Grain size effects on gas sensitivity of porous SnO₂-based elements. Sens. Actuators B: Chem. **3**(2), 147–155 (1991)
- 57. Yang, A., Tao, X., Wang, R., Lee, S., Surya, C.: Room temperature gas sensing properties of SnO₂/multiwall-carbon-nanotube composite nanofibers. Appl. Phys. Lett. **91**(13), 133110 (2007)
- 58. Zhu, J.J., Zhu, J.M., Liao, X.H., Fang, J.L., Zhou, M.G., Chen, H.Y.: Rapid synthesis of nanocrystalline SnO2 powders by microwave heating method. Mater. Lett. **53**(1-2), 12–19 (2002)